
# Interplay between γ′ precipitation, residual stress and strain-age cracking in CM247LC produced by powder bed fusion – laser beam

Materials & Design 270 (2026) 116955

Contents lists available at ScienceDirect

Materials & Design

journal homepage: www.elsevier.com/locate/matdes

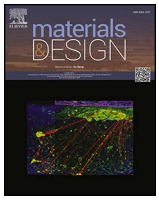

# Interplay between γ′ precipitation, residual stress and strain-age cracking in CM247LC produced by powder bed fusion – laser beam

Ahmed Fardan [a,*], Tatiana Mishurova [b], Severin Jakob [c], Guilherme Faria [d], Jakob Schröder [e], Alexander Evans [e], Mattias Thuvander [c], Håkan Brodin [a,f], Eduard Hryha [a]

[a] Department of Mechanical Engineering, Chalmers University of Technology, Göteborg 412 96, Sweden
[b] Helmholtz-Zentrum Berlin für Materialien und Energie (HZB), Berlin 12489, Germany
[c] Department of Physics and Astronomy, Chalmers University of Technology, Göteborg 412 96, Sweden
[d] Helmholtz-Zentrum Hereon, Institute of Materials Physics, Geesthacht 21502, Germany
[e] Bundesanstalt für Materialforschung und – Prüfung (BAM), Unter den Eichen 87, Berlin 12205, Germany
[f] Siemens Energy AB, Finspång 612 83, Sweden

ARTICLE INFO

*Keywords:*
Powder bed fusion–laser beam
CM247LC
Residual stress
Spinodal decomposition
Strain-age cracking
Non-weldable superalloy

ABSTRACT

Ni-base superalloys with high γ′ volume fraction, such as CM247LC, manufactured by powder bed fusion–laser beam (PBF–LB) are highly susceptible to strain-age cracking (SAC) due to the combination of process-induced residual stress (RS) and rapid γ′ precipitation during post-processing heat treatment. This work establishes a relationship between γ′ precipitation and RS relief across a matrix of ex-situ isothermal heat treatments (650–1050 °C, 1–8 h) to identify a candidate processing window for SAC mitigation in CM247LC. This is done using a correlative approach combining scanning electron microscopy, atom probe tomography and synchrotron X-ray diffraction. The as-built microstructure exhibits nano-scale spinodal-like clustering of Cr–Co-rich and Al-(Ni, Al, Ti, Ta, Hf)-rich regions, which evolve into well-defined γ′ precipitates above 750 °C, while RS relief is negligible at 650 °C, partial at 700 °C and substantial at ≥ 750 °C. Critically, heat treatment at 700 °C for 1–4 h provides partial RS relief without extensive γ′ precipitation and SAC, whereas prolonged holding or higher temperatures promote SAC. These findings establish a qualitative map of γ′ precipitation–RS relief–SAC, enabling design of post-processing heat treatments to mitigate SAC in PBF–LB processed high γ′ superalloys.

## 1. Introduction

Powder bed fusion – laser beam (PBF–LB) is an additive manufacturing technology that is capable of manufacturing complex geometries. Due to the design freedom, repair capabilities and printing-on demand, PBF–LB is used to manufacture high performance components, especially in the hot sections of gas turbines intended for use in aerospace and energy sectors [1,2]. Although there are several examples of successful implementations of complex components in easy to weld superalloys such as IN718, there is a limitation when it comes to difficult-to-process (non-weldable) superalloys containing high γ′ volume fractions such as CM247LC. This is due to the high cracking susceptibility of these alloys during PBF–LB processing and post-processing heat treatments [3]. The cracks that emerge during the PBF–LB processing are typically solidification cracks and can be mitigated through PBF–LB process optimization [4,5] along with hot isostatic pressing (HIP) [6,7]. However, strain-age cracking (SAC) that occurs in complex geometries after post-processing heat treatments is a major hindrance to the realization of reliable PBF–LB processed components [8,9].

SAC is the result of the combination of *1)* thermally induced stresses from the PBF–LB process and *2)* γ′ precipitation induced stresses [10,11]. The stresses are generated due to the localized melting and solidification of the layer-by-layer nature of the PBF–LB process. These are caused by the temperature gradient mechanism in combination with the shrinkage during cooling of the previous layer, which in turn is due to mechanical constraint caused by the previously solidified layer or build platform [12–14]. These gradients lead to high residual stress (RS) to be retained in the as-built PBF–LB components [15,16]. RS is relieved during post-processing heat treatment and involves holding the as-built PBF–LB part at a high temperature ($T/T_m > 0.7$, where $T_m$ is the melting

* Corresponding author.
*E-mail address:* fardan@chalmers.se (A. Fardan).

https://doi.org/10.1016/j.matdes.2026.116955
Received 11 March 2026; Received in revised form 19 August 2026; Accepted 1 September 2026
Available online 6 September 2026

temperature of the alloy) for a fixed duration [17,18]. However, during the heat-up ramp to the set-temperature, γ′ precipitation occurs that induces additional stress before achieving RS relief, ultimately triggering SAC [8]. This is particularly challenging for high γ′ alloys like IN738LC and CM247LC, where rapid γ′ precipitation kinetics (driven by the high Al + Ti content, > 5 wt%) makes it difficult to achieve RS relief without concurrent precipitation hardening and ductility loss [19–21].

Recent research has been directed towards either optimizing the PBF–LB process to minimize RS and suppress SAC for standard legacy alloys [4,5], or developing new or modified compositions with reduced SAC susceptibility [9,22]. This means that these modified alloys need to undergo rigorous testing and qualification before introduction in industrial applications. Therefore, there is still interest in minimizing SAC through fine-tuning the PBF–LB process and post–processing heat treatments for alloys like CM247LC. Substantial work has also been done on characterizing γ′ precipitation mechanisms and RS evolution in PBF–LB processed superalloys; however, these phenomena have rarely been studied together in a correlative framework. Previous studies [19,21] have focused on microstructural evolution to characterize γ′ precipitates, while RS measurements and relief kinetics have primarily been focused on alloys with sluggish precipitation kinetics such as IN625 [23] or IN718 [16]. Therefore, there is a need to understand the temporal interplay between γ′ precipitation and RS relief for high γ′ alloys like CM247LC to understand and mitigate SAC.

To address this gap, the current study employs a correlative characterization approach, combining scanning electron microscopy (SEM), atom probe tomography (APT), and synchrotron X-ray diffraction (S-XRD) to track γ′ precipitation and RS evolution in PBF–LB processed CM247LC. Isothermally heat-treated samples processed at temperatures of 650–1050 °C for 1–8 h were characterized ex-situ via SEM and APT, RS measured by S-XRD, and SAC assessed using cruciform geometries. This integrated approach provides a comprehensive map of the γ′ precipitation–RS relief–SAC interplay, enabling design of post-processing heat treatments to mitigate SAC in PBF–LB processed high γ′ Ni-base superalloys.

## 2. Material and methods

### 2.1. Powder, sample manufacturing and heat treatment

Gas-atomized CM247LC powder with a particle size range of 15 to 45 μm, supplied by Höganäs AB (Höganäs, Sweden), was used to manufacture the investigated samples. The powder's chemical composition, as provided by the supplier, is detailed in Table 1. An EOS M290 PBF–LB machine was used with optimized parameters from a previous study [4,24]. The laser power, scanning speed, hatch spacing, and layer thickness were 125 W, 1200 mm/s, 0.05 mm, and 0.03 mm, respectively. A stripe strategy with a 5 mm width, 0.12 mm overlap, and a 67° scan rotation was employed. The samples were separated from the build plate using electrical discharge machining (EDM). Note that EDM cutting can possibly change RS level, but the extent of stress relaxation reduces with the height of the built sample [25]. Therefore, the extent of stress relaxation can be assumed to be minimal for tall and bulkier samples.

Two sample geometries were printed: a cylinder (20 mm in height and 7 mm in diameter) and a cruciform (40 mm height × 30 mm wide × 10 mm thick). The cylinders were used primarily for microstructural analysis, while the cruciforms were used for RS evaluation (Fig. 1b), macro-cracking observations and partly for microstructure characterization. The cruciform geometry was selected because the sharp notch features provide localized stress concentration and have previously been demonstrated to promote strain-age cracking in PBF–LB CM247LC [8,9,24]. One cruciform sample per heat treatment condition was used throughout the study. Note that further information regarding the geometry and dimensions can be found in [24]. It is to be noted that the cruciform samples in their as-built condition contain micron-sized solidification cracks (crack density ~ 0.2 mm/mm$^2$), however no macro-sized strain-age cracks were visible near the notches when viewed under stereo optical microscope.

The cylindrical and cruciform samples were isothermally heat-treated in a Carbolite furnace (ceramic tube furnace in argon atmosphere (6 N purity)). Temperatures ranging from 650 °C to 1050 °C with 50 °C increment were chosen. For each heat treatment, the furnace was heated to the target temperature (heating rate of 10 °C/min) and allowed to stabilize for 1 h before placing the samples into the furnace on an alumina crucible. The furnace was then closed and then the samples were then removed after holding times of 1, 2, 4, and 8 h and were air-cooled. The start of the holding time was defined from the time at which the specimens were inserted into the preheated furnace. The purpose for air-cooling instead of quenching or forced air cooling was mainly done to avoid inducing any additional stress. The cooling rate during air cooling was not measured. Note that there was no continuous temperature monitoring of the samples during the heat treatments, but the furnace was previously calibrated.

The cruciform samples were investigated for strain-age cracks near the notches using stereo optical microscope as well as on polished cross-sections using a light optical microscope (LOM). Cracks were identified as continuous, dark linear features extending from or near the notch region in the optical micrographs. Note that no sectioning of the cruciform was done prior to sample preparation for LOM. Instead, the cruciform was mounted and ground until the rough surface (containing partially sintered/melted powders attached) was removed and followed by polishing. The grinding and polishing steps were performed as outlined in Section 2.3. The LOM observations were used primarily to document the presence of cracks, and no attempts were made to quantify the crack density, length or depth of the strain-age cracks.

### 2.2. Synchrotron X-ray diffraction measurements

Energy dispersive synchrotron X-ray diffraction (S-XRD) measurements were performed at the Hereon-operated white beam engineering materials science beamline P61A at the Deutsches Elektronen-Synchrotron (DESY) in Hamburg, Germany [26]. A simplified illustration of the basic instrument principle in reflection mode is shown in Fig. 1a. The energy dispersive detector measures the energy ($E^{hkl}$) of the X-rays diffracted by the sample at a fixed diffraction angle $\theta$. In such a case, Bragg's law can be rewritten in terms of photon energy with $h$ being the Planck's constant, $c$ being the speed of light and $d^{hkl}$ being the lattice spacing [27]:

$$d^{hkl} = \frac{h \times c}{2\sin\theta} \times \frac{1}{E^{hkl}} \quad (1)$$

The incoming beam was narrowed by the vertical and horizontal slits to a 250 × 250 μm$^2$ cross section. The diffracted beam was narrowed to 50 × 10000 μm$^2$ using further slits. The $\sin^2\psi$ method combined with the modified multiwavelength method [28] was used for evaluation of the RS at the sub-surface region on samples with as-built surfaces (without

**Table 1**
Chemical composition of the CM247LC powder used in this study.

| | Cr | Co | Mo | C | W | Hf | Ta | Ti | Al | Zr | B | Si | O | Ni |
|---|---|---|---|---|---|---|---|---|---|---|---|---|---|---|
| wt.% | 8 | 9.3 | 0.5 | 0.06 | 9.7 | 1.3 | 3.2 | 0.8 | 5.6 | 0.009 | 0.01 | 0.08 | 0.01 | Bal. |
| at.% | 9.20 | 9.43 | 0.31 | 0.30 | 3.15 | 0.44 | 1.06 | 1 | 12.40 | 0.006 | 0.06 | 0.17 | 0.04 | Bal. |

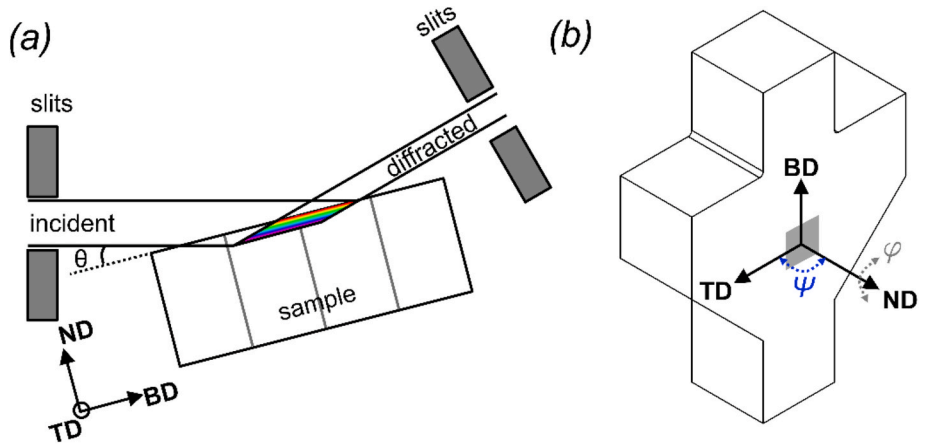


**Fig. 1.** Schematic of the measurement principle for energy-dispersive synchrotron XRD (a) Set-up indicating the relationship between incident and diffracted beam, (b) schematic of the sample showing the location of the measurement indicated by the gray box.

electrolytic polishing) [29]. It is assumed that the stresses in the normal direction (ND) to the surface are zero, i.e plane stress. The measurements were performed at the lateral surface of the samples along the build direction (BD) in the center of the sample, as indicated in Fig. 1b. One sample per heat treatment condition was measured due to the limited time frame and number of samples. The specimens were mounted on the Eulerian cradle in reflection mode, and $\psi$ was tilted in the range of $-75^\circ$ to $75^\circ$ in $5^\circ$ steps ($\psi$ is defined as the tilt angle between the surface normal and the diffraction vector).

The wide energy spectrum of the white beam provides depth resolution due to the different energies yielding information from different depths ($\tau$). In this study, the (311) reflection is used to assess the residual stress, which comes from a maximum information depth of $\sim$ 50 μm. Because γ and γ′ have closely related lattice structures, their fundamental diffraction peaks can overlap, particularly as γ′ precipitation develops. The (311) reflection was therefore treated as an effective response of the γ/γ′ microstructure rather than as a phase-specific measurement. Prior to the measurements, calibration was performed using a NIST Silicon powder, resulting in a diffraction angle of $2\theta = 8.54^\circ$. The information depth ($\tau$) is given by $\mu$ denoting the linear absorption coefficient [30]:

$$\tau^{hkl} = \frac{\sin\theta}{2\mu} \times \cos\psi \tag{2}$$

Data analysis was performed in the open-source software P61A: Viewer developed at the P61A beamline, using a pseudo-Voigt function [31]. Peaks below 100 counts were excluded from the subsequent RS analysis. The X-ray diffraction elastic constants (DECs) used for stress calculations were obtained for the (311) reflection according to Reuss model using ISODEC [32]: $s_1 = -1.44 \times 10^{-6}$ MPa$^{-1}$ and $1/2\ s_2 = 6.95 \times 10^{-6}$ MPa$^{-1}$ using single crystal elastic constants for CM247LC reported in [33].

### 2.3. Sample characterization (SEM and APT)

Microstructural investigations were carried out on cross-sections perpendicular to the build direction extracted from the cylindrical samples. The samples were mounted in conductive resin suitable for SEM. This was followed by sequential grinding with 1000, 1200, 2000, and 4000-grit SiC papers. Polishing was then performed using a 3 μm diamond suspension on a taffeta woven wool surface (MD-Mol by Struers), followed by a 1 μm polishing step. Finally, a 0.05 μm colloidal silica (OPS) suspension was used to remove any residual deformation from previous grinding and polishing steps. The prepared cross-sections were examined using a Zeiss Gemini 450 SEM (Carl Zeiss Microscopy GmbH, Oberkochen, Germany) with secondary (SE), in-lens, and backscattered electrons (BSE).

Some of the SEM micrographs were acquired in the SE or in-lens mode in etched condition to analyze the solidification cells and the γ/γ′ microstructure. The etching was performed electrolytically using a 10 % oxalic acid aqueous solution with 3 V for 5–10 s. This etches the dendritic core or γ matrix leaving the interdendritic regions or γ′ precipitates.

Sample blanks for APT were fabricated by cutting and grinding to achieve dimensions of $0.3 \times 0.3 \times 10$ mm$^3$ either from the cylindrical samples or the cruciforms. Needle-shaped specimens were prepared by a two-step electropolishing process in 10 % and 2 % perchloric acid, respectively [34]. APT specimens were measured in a LEAP 6000 XR (CAMECA Instruments, Madison, WI, USA) in laser-mode, utilizing a laser with a wavelength of 257.5 nm. The measurements were conducted at a test temperature of 50 K, the laser pulse energy was set to 30 pJ at a repetition rate between 130 and 315 kHz and the target detection rates were between 0.5 and 3 %. Reconstructions were made in the commercial software AP Suite 6.3 (CAMECA) using the voltage method and an image compression factor of 1.65, a field factor of 4.0 and an estimated field of 30 V/nm. Error bars in proxigrams represent counting statistics only; systematic uncertainties from background algorithms, unnoticed overlaps of molecular ions, surface diffusion, evaporation between pulses etc. are not included. At least one APT tip was successfully analyzed for each reported heat-treatment condition. Additional acquisitions were terminated in cases of premature specimen fracture or when comparable compositional trends were obtained.

### 2.4. Thermo-Calc calculations

Thermo-Calc 2025b with TCNI13 database was used to calculate the equilibrium composition of γ matrix and γ′ precursor/precipitate at temperatures ranging from 650 °C to 1050 °C.

## 3. Results

### 3.1. Microstructural evolution (SEM)

The as-built microstructure perpendicular to the build direction (Fig. 2) exhibits a cellular-like structure consisting of primary dendrites, typical of PBF–LB processed CM247LC. The BSE-SEM micrograph (Fig. 2a) recorded on a sample in unetched condition exhibits varying contrast for the dendrites with the size of 703 ± 193 nm, arising from the difference in channeling conditions achieved due to differences in misorientation [35,36]. The inset in Fig. 2a shows magnified dendritic cores containing visible dislocations. Interdendritic boundaries (red

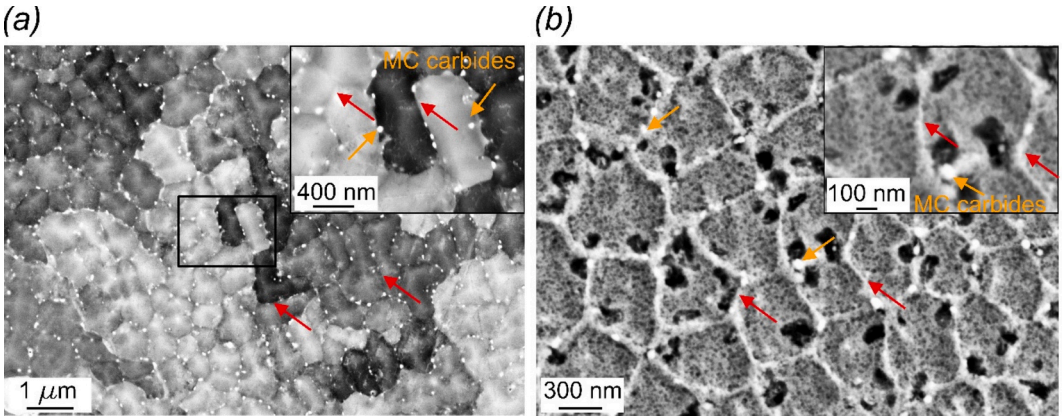


**Fig. 2.** As-built microstructure (a) BSE-SEM image showing cellular structures. Inset shows the magnified view of the region. Arrows indicate primary MC carbides, (b) SE-SEM image obtained in the etched condition. Red arrows show interdendritic regions. Orange arrows indicate the MC carbides. (For interpretation of the references to colour in this figure legend, the reader is referred to the web version of this article.)

arrows) contain bright MC carbides (yellow arrows) [4,37]. After electrolytic etching in 10 % oxalic acid (Fig. 2b), the interdendritic regions remain visible (red arrows), and MC carbides persist (yellow arrows). This etched as-built microstructure serves as a baseline for comparison with heat-treated conditions.

The microstructures of samples isothermally heat-treated for 1 h at 650 °C, 850 °C and 1050 °C are shown in Fig. 3. Microstructures for 2, 4 and 8 h are provided in Fig. S1 in the Supplementary information. From Fig. 3a and d, it can be observed that the 650 °C condition has interdendritic boundaries (marked with red arrows) similar to the as-built microstructure (Fig. 2). However, no clear indication of γ′ precipitates was found. The 850 °C condition (Fig. 3b and e) has fine irregular γ′ precipitates (size: 92 ± 28 nm) with continuous precipitates in the interdendritic boundaries. These continuous γ′ precipitates are analogous to grain boundary γ′ observed in sub-solvus solution heat treated PBF–LB superalloys [38]. Finally, the 1050 °C (Fig. 3c and f) condition is found to have coarse γ′ precipitates (size: 245 ± 66 nm). Note that the γ′ precipitate size measurements were performed on three SEM fields obtained at magnification of 100,000 × and 30,000 × for 850 °C and 1050 °C, respectively.

The SEM results demonstrate that γ′ precipitation occurs at 850 °C. To capture the transition between 650 °C and 850 °C, APT was employed to characterize intermediate temperature conditions and to elucidate the γ′ formation mechanism.

### 3.2. Compositional evolution and γ′ formation mechanism

APT reconstructions for the as-built and all the 1 h isothermally heat-treated samples are shown in Fig. 4. To quantify the compositional evolution, two complementary statistical tools were employed, namely radial distribution functions (RDFs) and proxigrams (Fig. 5).

RDF is a statistical tool that can confirm compositional variations.

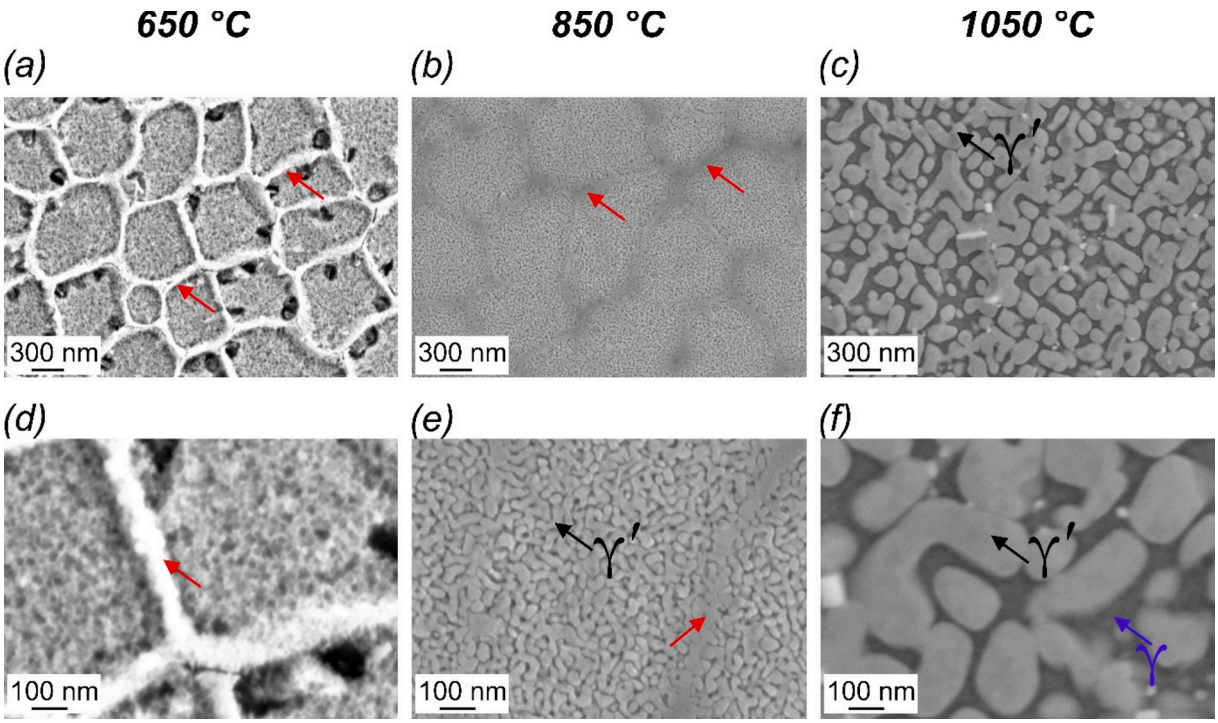


**Fig. 3.** SEM micrographs of etched microstructure for samples isothermally heat treated at (a) 650 °C, (b) 850 °C and (c) 1050 °C for 1 h. (d)-(f) are magnified micrographs of (a)-(c). Red arrows indicate interdendritic boundaries. Black arrows indicate γ′ precipitates. The blue arrow indicates γ matrix. (For interpretation of the references to colour in this figure legend, the reader is referred to the web version of this article.)

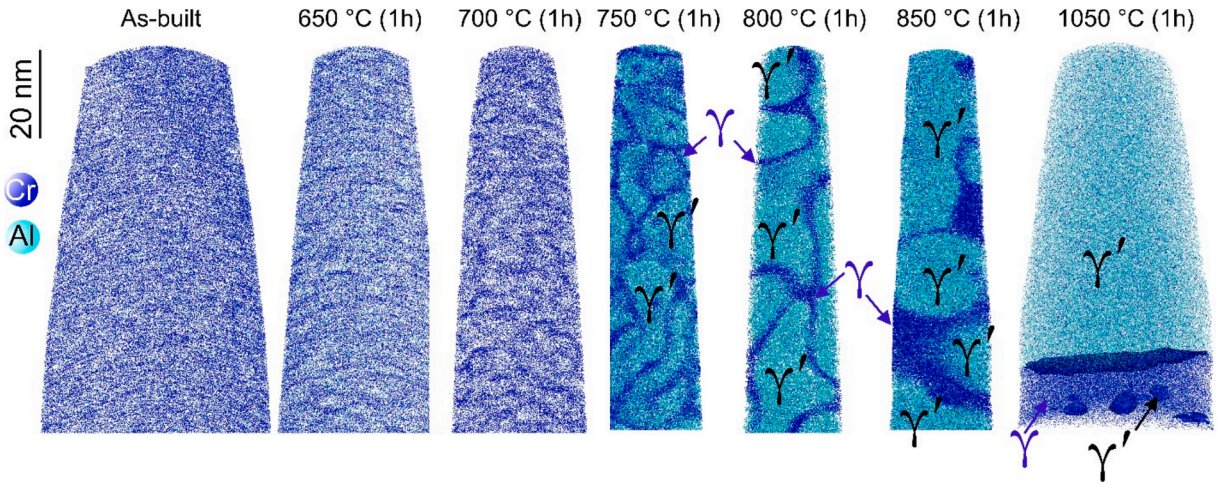


**Fig. 4.** APT reconstructions for as-built and isothermally heat-treated samples from 650 °C to 1050 °C for 1 h. The Cr and Al atoms are represented as spheres. 1050 °C additionally is represented with Cr *iso*-surface (15 at. %) to highlight the γ channel and fine γ′.

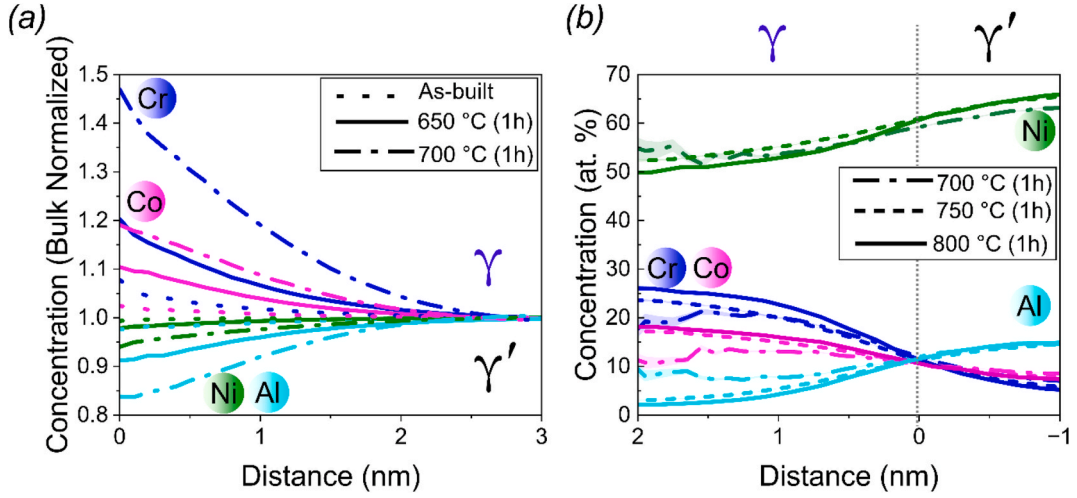


**Fig. 5.** (a) Radial distribution function (RDF) for as-built, 650 °C (1 h) and 700 °C (1 h) conditions using Cr atoms as reference, (b) Proxigrams for 700 °C (1 h), 750 °C (1 h) and 800 °C (1 h) obtained with reference to an *iso*-concentration surface of 11.5 at.% Cr, 12 at.% Cr and 13.5 at.% Cr, respectively. Error bars in (b) indicate statistical uncertainties are shown as lines with filled transparent color and correspond to the 2σ error.

The neighborhood solute atoms surrounding a species (in this study Cr) are counted and an average composition of each element as a function of radial distance to this particular species is calculated [39–41]. Proxigrams, or proximity histograms, display the average concentration as a function of the distance to an *iso*-concentration surface (in this study Cr) made for a user-determined threshold (10–15 at. %). The reason for choosing to use RDF for as-built, 650 °C (1 h) and 700 °C (1 h) is the lack of clear γ′ precipitates but instead presence of clustering in these conditions. Proxigrams were used for conditions ≥ 750 °C where Cr-rich/Al-rich interfaces could be observed better from the reconstructions.

APT reconstructions (Fig. 4) and RDF analysis (Fig. 5a) reveal that as-built, heat treated at 650 °C (1 h), and 700 °C (1 h) samples contain two compositionally distinct clustering zones: a Cr-rich zone and a Cr-depleted (Al-rich) zone. The RDF shows that γ-forming elements (Cr, Co) partition into Cr-rich zones, while γ′-forming elements (Ni, Al) partition into Al-rich zones. This nanoscale compositional modulation is consistent with spinodal decomposition mechanism, as reported previously for PBF–LB processed superalloys [4,19,21]. With increasing temperatures from as-built to 700 °C, clustering intensifies: Cr and Co further enrich Cr-rich regions, while Ni and Al enrich Al-rich regions (Fig. 5a). At 700 °C (1 h), the interface between these regions becomes more distinct than at 650 °C or as-built, though it remains diffuse (~3–4 nm width, as shown in Fig. 5b). Proxigrams for 700 °C (1 h), 750 °C (1 h), and 800 °C (1 h) (Fig. 5b) reveal progressive interface sharpening with increasing temperature. At 750 °C (1 h), the Al-rich regions coarsen, and the interface width narrows to ~ 2–3 nm with steeper concentration gradients. For 800 °C (1 h), a well-defined γ/γ′ interface (~1–2 nm width) is established, with concentration profiles approaching a step-function behavior characteristic of ordered γ′ precipitates.

The shift from non-equilibrium clustering to equilibrium-like γ/γ′ partitioning is quantified in Fig. 6, which shows average compositions of Cr-rich zones (γ phase) and Al-rich zones (γ′ precipitate/precursor) delineated by Cr *iso*-surfaces. Full compositional data and Thermo-Calc equilibrium predictions are provided in Tables S1 and S2 (in Supplementary information). The Cr *iso*-surface threshold values were chosen for each proxigram such that it corresponded to the concentration at which the raw compositional profile crossed the same value (i.e., the point of zero distance in the resulting proxigram), ensuring the *iso*-surface was anchored to the true γ/γ′(−precursor) interface rather than displaced toward either phase. The resulting threshold increased monotonically with heat-treatment temperature, from 10.5 at.% (as-built, 650 °C) to 15 at.% (850 °C, 1050 °C), see Table S3, consistent with progressively stronger Cr/Co and Ni/Al partitioning at higher temperatures. In the as-built condition, both γ and γ′ regions exhibit

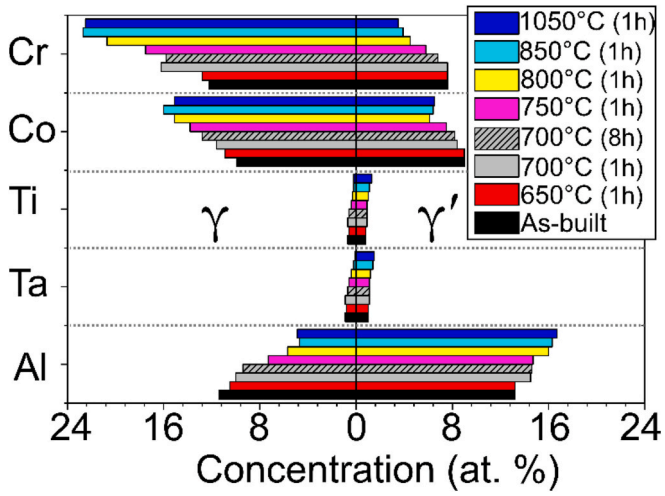


**Fig. 6.** Elemental partitioning between γ and γ′ phases obtained from APT for selected elements. Additional information is found in Table S1 and Table S2 in Supplementary information.

compositions close to the nominal powder composition, with minimal partitioning. With increasing temperature, the γ matrix becomes progressively enriched in Cr and Co while depleting in Al, Ta, and Ti. Conversely, γ′ precipitates show complementary enrichment in Al, Ta, and Ti with depletion in Cr and Co. This trend is most pronounced for Cr and Al. In the γ phase, Cr increases from 12.2 at.% (as-built) to 22.5 at.% (1050 °C); Al decreases from 11.4 at.% to 4.9 at.%. In contrast in γ′ precursor/precipitate, Al increases from 12.8 at.% (as-built) to 16.7 at.% (1050 °C); Cr decreases from 8.4 at.% to 3.5 at.%.

The Hf concentrations measured by APT (Tables S1 and S2 in Supplementary information) are consistently lower than the nominal powder composition and show fluctuating partitioning behavior. This is attributed to the high melting point of Hf, low diffusivity, and strong tendency to segregate to interdendritic and grain boundaries [42], making it underrepresented in APT sampling from dendritic cores. Notably, significant γ′ enrichment of Hf occurs only at 1050 °C (1 h), where the γ′ composition (measured from APT) approaches equilibrium, consistent with Thermo-Calc predictions and fully heat-treated PBF-LB processed CM247LC by Adegoke *et al.* [43]. Additionally, fine γ′ precipitates captured at 1050 °C (1 h) exhibit lower Al, Ti, and Ta content and higher Cr and Co content compared to coarse γ′, partially agreeing with observations in cast CM247LC by Babu *et al.* [44].

Since SAC occurred at 700 °C after 8 h (shown later in Fig. 9), APT was performed on this condition and compared with 700 °C (1 h) (Fig. 7). The APT reconstruction (Fig. 7a) shows coarsening of Al-rich clusters after 8 h. An RDF analysis (Fig. 7b) confirms enhanced partitioning: Cr and Co enrichment in γ-rich regions increases from 1.45 and 1.25 bulk normalized concentration for (1 h) to 1.50 and 1.30 (8 h), respectively. In parallel, Al enrichment in γ′-precursor regions increases for 8 h when compared to 1 h. However, the proxigram (Fig. 7c) reveals that the γ/γ′ interface remains diffuse (~3–4 nm) even after 8 h, with limited changes compared to 1 h. This indicates that at 700 °C, the microstructure undergoes spinodal-like clustering and coarsening but has not transitioned to the ordering stage required for fully developed γ′ precipitates. It must be noted that the APT observations are from the bulk i.e. the dendrite core. Interdendritic and grain boundary regions were not sampled in this analysis and could show a difference in precipitation behavior.

### 3.3. Residual stress evolution

The evolution of sub-surface RS along the build direction as a function of heat treatment temperature and duration is presented in Fig. 8.

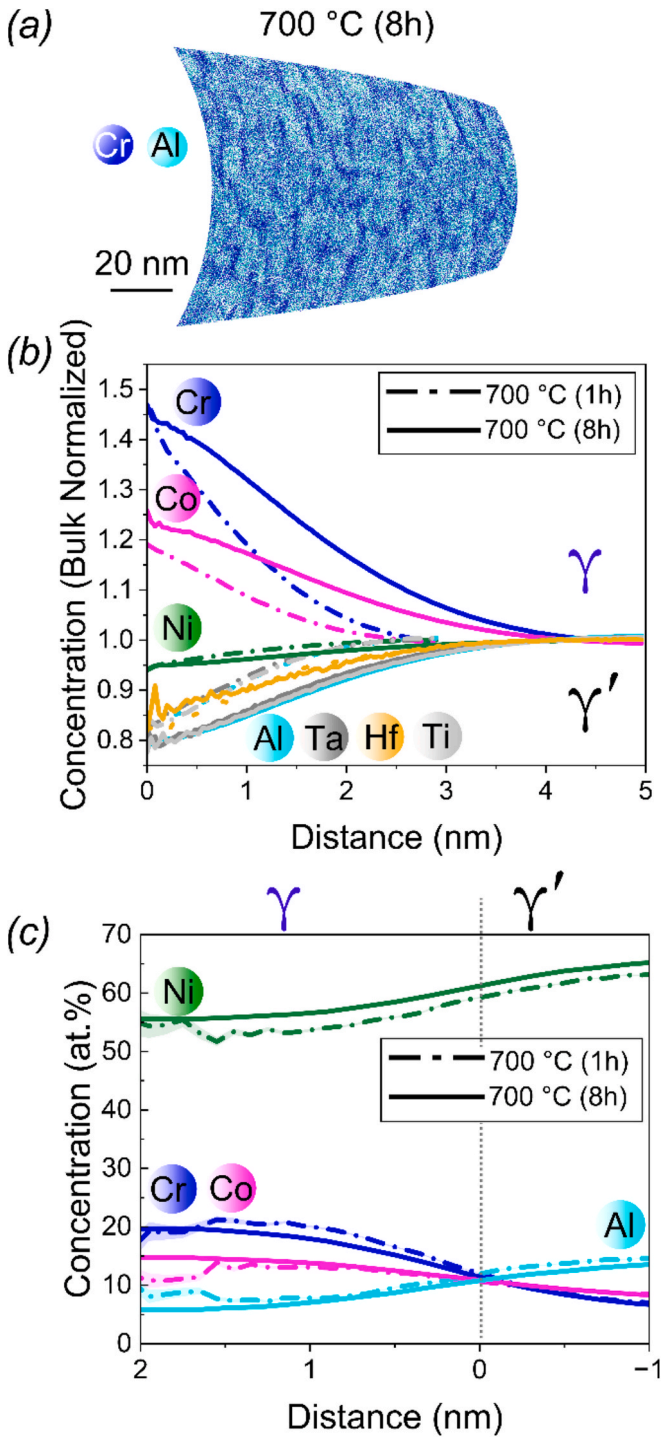


**Fig. 7.** (a) APT of 700 °C (8 h) sample, (b) RDF of 700 °C heat treated for 1 h and 8 h, (c) Proxigram of 700 °C (1 h) and 700 °C (8 h) obtained with reference to an *iso*-concentration surface of 12 at.% Cr. Error bars in (b) indicate statistical uncertainties are shown as lines with filled color and correspond to the 2σ error.

The as-built condition exhibits high tensile RS of 465 ± 41 MPa, characteristic of PBF–LB processed samples. It should be noted that these values are measured at a maximum information depth of ~50 μm; previous studies reported higher tensile stresses (reaching > 700–800 MPa) at a depth of 100–200 μm from the as-built surface [4,16].

At 650 °C, negligible RS relief occurs across all durations (1–8 h), with RS fluctuating between 378 ± 9 MPa and 494 ± 43 MPa which is comparable to the as-built state. This indicates insufficient thermal

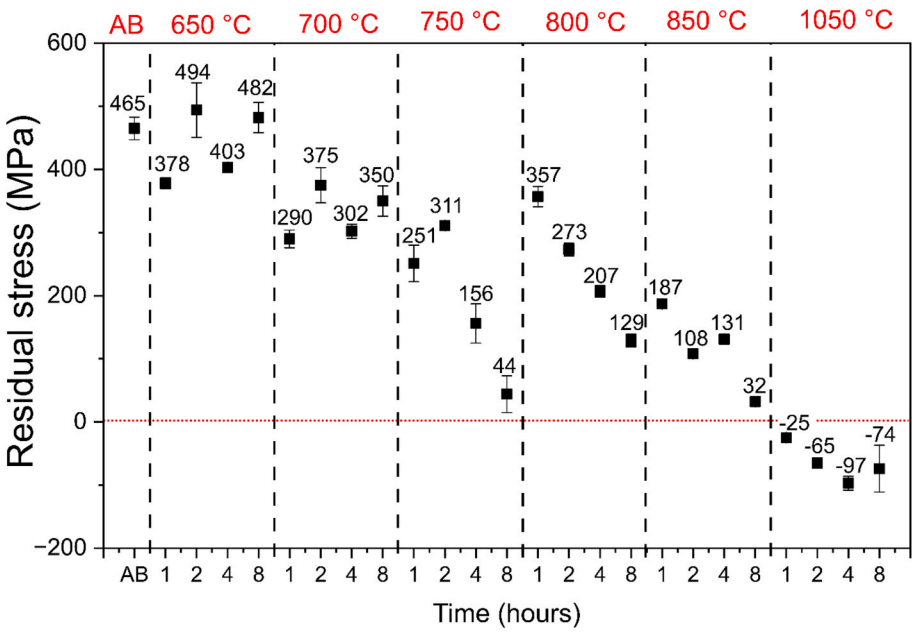


**Fig. 8.** Evolution of subsurface RS along build direction for as-built (AB) and heat-treated conditions obtained using (311) reflection. The error bars indicate fitting uncertainty.

activation for stress relaxation mechanisms at 650 °C, consistent with the absence of γ′ precipitation (Fig. 4). At intermediate temperatures (700–800 °C), complex RS evolution is observed. Heat treatments for 1 h at, 700 °C and 750 °C allow to achieve moderate RS relief (290 ± 14 MPa and 251 ± 29 MPa, respectively). However, an anomalous trend emerges at 800 °C (1 h), where RS increases to 357 ± 16 MPa which is higher than both 700 °C and 750 °C despite the elevated temperature. This counter-intuitive behavior reflects competing mechanisms: thermal stress relaxation versus precipitation-induced stress generation. For 8-hour treatments, behavior diverges markedly. At 700 °C (8 h), RS relief stagnates at 350 ± 24 MPa, showing minimal improvement over treatment for 1 h. In contrast, 750 °C (8 h) and 800 °C (8 h) exhibit substantial RS relief (44 ± 29 MPa and 129 ± 10 MPa, respectively).

At 850 °C, progressive RS relief occurs with increasing duration, transitioning from 187 ± 6 MPa (1 h) → 32 ± 3 MPa (8 h). Finally, at 1050 °C near-complete RS relief is achieved within 1 h (−25 ± 7 MPa), transitioning to low compressive stresses with longer durations (−65 ± 12 MPa at 2 h; −74 ± 37 MPa at 8 h). The surface compressive stresses at 1050 °C arise from differential thermal contraction during cooling where the surface cools faster than the bulk, and its shrinkage is constrained by the interior, inducing compression stresses. This phenomenon is well-documented in solution heat-treated superalloys and reflects complete stress redistribution at near-solvus temperatures [17,23].

The RS evolution (Fig. 8) reveals a critical processing window at 700 °C for 1–4 h which achieves partial RS relief (~38 %, 19 %, and 35 % reduction at 1, 2, and 4 h when compared to as-built) without

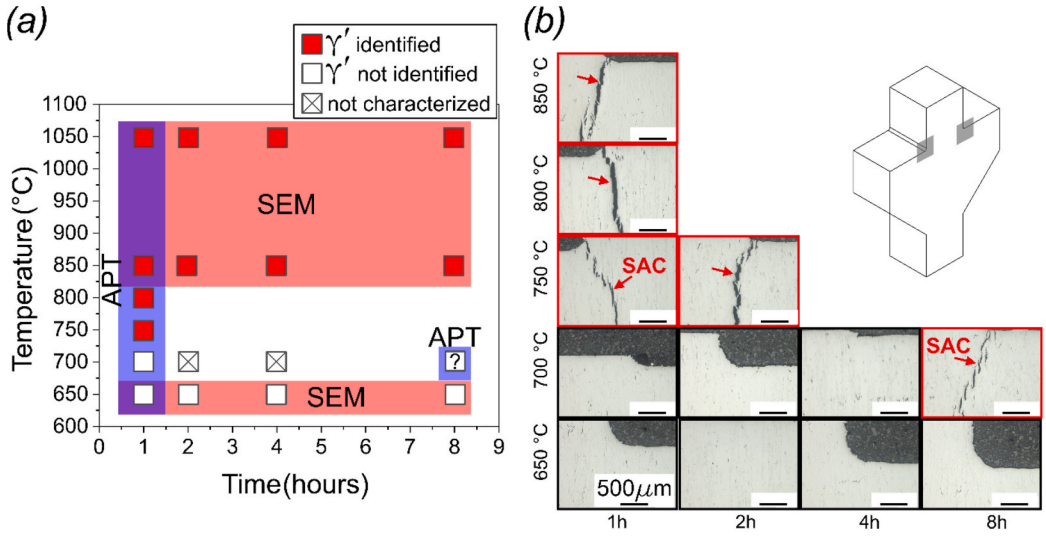


**Fig. 9.** (a) Qualitative temperature–time plot indicating the identification of γ′ as well as strain-age cracking (SAC) for CM247LC produced by PBF–LB. The question mark (?) indicates the condition where γ′ was not clearly identified but SAC occurred. (b) Optical micrograph of the polished cross-section for selected temperature–time conditions and the cruciform sketch indicating the locations where micrographs were obtained. The characterization technique (SEM or APT) used to identify the γ′ precipitates are marked using colored boxes. Red box indicates specimens characterized using SEM. Blue box indicates conditions characterized using APT. Purple color (red and blue overlap) indicates specimens characterized using both SEM and APT. Note that two specimens were not characterized for γ′. (For interpretation of the references to colour in this figure legend, the reader is referred to the web version of this article.)

extensive γ′ precipitation, as confirmed by APT (Figs. 4–7). The non-monotonic variation also indicates a specimen-to-specimen variability due to the limited statistics due to measurement on one sample along with the measurements in reflection mode. Therefore, there is a need for further work to confirm the RS relief at 700 °C for 1–4 h and possibly transmission mode experiments to measure RS in the bulk of the sample.

### 3.4. Correlation: γ′ precipitation and SAC

The combined microstructural and RS findings are summarized in Fig. 9a, which maps heat treatment conditions as a function of temperature and time. Solid (red) boxes indicate conditions where γ′ precipitates were identified (by SEM and/or APT), while empty boxes indicate early-stage clustering where γ′ was not clearly identified. Note that for two heat treatment conditions no characterization for γ′ precipitates were performed. Fig. 9b shows representative optical micrographs of polished cross-sections near stress-concentrator notches, revealing SAC for certain conditions. The correlation between γ′ formation, RS evolution, and SAC occurrence across all conditions is discussed in *Section 4*.

## 4. Discussion

During post-build heat treatment of a γ′ precipitate strengthened superalloy produced by PBF–LB, two thermally-activated phenomena occur concurrently: *1)* γ′ precipitation either through classical nucleation and growth or through spinodal decomposition [19,21,43] and *2)* RS relief or generation of additional stresses due to γ′ precipitation [8]. In high γ′ Ni-base superalloys like CM247LC (equilibrium γ′ volume fraction of ~ 60–70 %), both processes occur in overlapping temperature ranges, making it challenging to decouple them. Understanding these mechanisms is critical to identifying a temperature window that achieves partial RS relief before extensive γ′ precipitation, thereby enabling industrial-scale post-processing of PBF–LB processed superalloys without SAC.

The as-built CM247LC microstructure (Fig. 4a) lacks discrete γ′ precipitates, consistent with the extremely rapid cooling rates of PBF–LB (~$10^5$–$10^6$ °C/s) [45,46] that suppress diffusional partitioning and chemical ordering during solidification. Instead, APT reveals two compositionally distinct nanoscale zones: Cr-rich zones (enriched in Cr and Co) and Al-rich zones (enriched in Ni, Al, Ti, Ta, and Hf). This compositional modulation is consistent with spinodal decomposition mechanism, which is a continuous phase separation mechanism occurring in thermodynamically unstable regions where the curvature of the free energy curve is negative, enabling spontaneous compositional fluctuations to grow without an activation barrier [47]. Similar clustering has been reported in as-built CM247LC by Fardan *et al.* [4] and Adegoke *et al.* [43], IN738LC by Schulz *et al.* [19], and RR1000 atomized powders by Collins *et al.* [21]. It is important to distinguish this clustering from fully formed γ′ precipitates. While some studies [48,49] have reported γ′ presence in as-built high γ′ alloys (CM247LC, IN713LC) using TEM, these precipitates were predominantly localized at interdendritic regions where solute segregation (Al, Ti, Ta) during solidification locally exceeds the critical composition for γ′ formation. The APT measurements in this study, sampled from dendritic cores, capture the bulk behavior and show no discrete γ′ precipitates in the as-built state. However, crystallographic confirmation of the ordered $L1_2$ structure was not performed.

Heat treatment at 650 °C and 700 °C intensifies partitioning of respective elements in the Cr-rich and Al-rich zones, respectively. At 750 °C (1 h), proxigrams reveal interface sharpening (~2–3 nm) and steeper concentration gradients (Fig. 5b), consistent with progressively stronger chemical partitioning. At 800 °C (1 h), a well-defined γ/γ′ interface (~1–2 nm) is established. The compositions of γ and γ′ progressively approach Thermo-Calc equilibrium predictions at 700 °C (Fig. 6, Tables S1 and S2) and experimentally measured values for fully heat-treated CM247LC [43]. The extremely high cooling rates achieved during PBF–LB leads to the supersaturated solution which along with the complex thermal history likely leads to compositional variations [4]. In comparison, the cooling rates of ~ $10^3$ °C/s achieved in [50] for cast CM247LC allow for complete elemental partitioning with composition of γ and γ′ phases closer to the equilibrium condition. The present study indicates that PBF–LB CM247LC is consistent with a spinodal decomposition pathway, with γ′ precipitates observed at temperatures ≥ 750 °C where sufficient thermal activation enables atomic rearrangement into the $L1_2$ structure.

Concurrently with the microstructural evolution, the RS relief progresses through distinct temperature-dependent regimes. RS relief in metallic materials occurs via thermally-activated mechanisms including dislocation glide, dislocation climb, recovery, and diffusional creep [51]. At 650 °C, negligible RS relief occurs even after 8 h (Fig. 8), despite spinodal-like clustering (Fig. 4). This indicates insufficient thermal energy to activate stress relaxation mechanisms, as the homologous temperature $T/T_m \approx 0.56$ is below the threshold ($T/T_m$ of ~ 0.6–0.7) for diffusion-controlled creep in nickel-based superalloys [52]. Please note that $T_m$ refers to the melting point of CM247LC and is taken as 1380 °C (1653 K) based on DSC (differential scanning calorimetry) measurements by Bassini *et al.* [7]. At 700 °C (1 h) and 750 °C (1 h), moderate RS relief is achieved, representing ~ 35–45 % reduction from the as-built state (465 MPa). This relief occurs via thermally-activated dislocation processes enabled by sufficient diffusivity at $T/T_m \approx 0.58$–$0.60$. Critically, at 700 °C, RS relief occurs without concurrent ordered γ′ precipitation (Figs. 4–7), as the microstructure remains in the spinodal-like clustering regime. This decoupling of RS relief from precipitation hardening is the key to avoiding SAC.

An unexpected observation is that 800 °C (1 h) exhibits higher RS than 700 °C and 750 °C (1 h). This behavior possibly suggests competing mechanisms: thermal stress relaxation versus precipitation-induced stress generation. It is likely that at 800 °C the coherency strain associated with γ/γ′ lattice misfit (~0.5–1.0 % [53]) possibly generates internal stresses that partially offset the thermally-driven RS relief [54]. Additionally, the RS relief observed for 750 °C and 800 °C (8 h) conditions could involve precipitation-assisted creep, where γ′ precipitates initially generate coherency stresses but subsequently facilitate dislocation climb and enhanced creep rates through localized stress concentration at γ/γ′ interfaces, ultimately enabling greater overall RS relief [55]. At 850 °C and 1050 °C, progressive and near-complete RS relief occurs, respectively, as thermal activation becomes dominant and γ′ precipitates coarsen (at 1050 °C), reducing coherency stress contributions. However, it must be noted that there is possibly specimen-to-specimen variability, limited statistics from the reflection-mode RS measurement and γ/γ′ peak overlap which could have an effect, indicating the need for further work. Furthermore, there is a need for in-situ heating experiments using high energy synchrotron X-ray to study the evolution of the coherency stresses generated during γ′ precipitation. And if the coherency stresses contribute to the proposed SAC mechanism.

SAC occurs when the combined stress state of RS from PBF–LB plus precipitation-induced stress possibly exceeds the local strength and/or ductility of the material, particularly at stress concentrators such as notches, geometric discontinuities, or grain boundaries [8–11]. Because RS was measured after ex-situ heat treatment, the values represent the remaining sub-surface RS after heat treatment and potentially SAC which could have potentially led to stress relaxation and redistribution of local stresses. It is to be further noted that the RS measurements reported in the paper were performed away from the notch (and SAC) which could have different local stresses. However, the critical insight from this study is that SAC susceptibility correlates with the relationship between RS relief and γ′ precipitation. Three distinct regimes emerge from Fig. 8 and Fig. 9a:

- Regime I: At 650 °C, spinodal-like clustering intensifies but does not transition to ordered γ′, and thermal activation is insufficient for RS relief. The material remains in its stressed as-built state (~400–500 MPa) but does not crack because strengthening and/or stresses from precipitation is minimal and insufficient to cause SAC.
- Regime II: At 700 °C for 1–4 h, partial RS relief occurs via thermally-activated processes, while the microstructure remains in the spinodal-like clustering regime. The absence of chemical ordering means precipitation strengthening is limited, and no SAC occurs in this regime (Fig. 9b), indicating that this is possibly a candidate processing window for partial stress-relief annealing.
- Regime III: At 700 °C (8 h) and ≥ 750 °C, SAC becomes prevalent. At 700 °C (8 h), extended aging promotes sufficient cluster coarsening and possible local ordering particularly at interdendritic and grain boundaries where solute segregation can lead to relatively rapid γ′ formation compared to the bulk (dendrite core).

To verify the additional strengthening due to precipitation and possible ductility loss, suitable further work would be to perform mechanical testing for the different heat treatment conditions. Additionally, note that the RS was measured ex-situ (after heat treatment) and cracking that occurred for certain heat treatment conditions could have resulted in stress relaxation and redistribution. And the verification of this relaxation and/or redistribution requires local mapping of stresses closer to the notches through transmission-mode synchrotron experiments.

For 700 °C (8 h), APT from dendritic cores shows limited interface sharpening (Fig. 7c), however SAC occurs (Fig. 9b), suggesting that either *1)* heterogeneous γ′ precipitation at boundaries provides localized strengthening, or *2)* coarsened spinodal-like clusters generate sufficient hardening to reduce ductility when combined with stress concentrators and retained RS (~300 MPa). At ≥ 750 °C, rapid γ′ formation generates coherency stresses, strengthens the matrix, and reduces ductility. When superimposed on retained RS (especially at 800 °C where RS relief is incomplete at 1 h, Fig. 8), the material becomes highly susceptible to SAC. Cracks nucleate at stress concentrators (Fig. 9b) where local stresses exceed the ductility of the precipitation-hardened material.

The 700–750 °C window for RS relief without extensive γ′ precipitation aligns with prior studies on both wrought and PBF–LB superalloys (such as IN625 and IN718) [23,55,56], where stress-relief annealing is performed in similar temperature ranges to enable diffusional creep without triggering precipitation hardening. However, PBF–LB materials present additional complexity due to: *1)* higher initial RS, *2)* fine-scale microstructure with high dislocation density, and *3)* spinodal-like clustering that can coarsen and order more rapidly than conventionally processed microstructures. This explains why the candidate processing window is narrower (700 °C, 1–4 h) compared to wrought materials. The findings indicate possibly a processing window for partial stress-relief annealing of PBF–LB CM247LC: 700 °C for 2–4 h, without triggering SAC. This pre-treatment can be integrated into a multi-step heat treatment, preferably in HIP to minimize SAC susceptibility. Additionally, there is a need for alternative strategies, and a notable one is modifying the alloy composition to suppress γ′ kinetics, volume fraction or lattice misfit which can minimize SAC. Furthermore, modifying RS accumulation and distribution through a combination of modified scanning strategies and/or build-plate pre-heating is also a viable option without modifying the composition.

This study focused on dendritic core microstructure characterized via APT. Future work should include site-specific APT at interdendritic and grain boundaries to confirm whether heterogeneous γ′ precipitation occurs in these regions at 700 °C (8 h). Additionally, a separate dedicated study using in-situ synchrotron XRD or neutron diffraction during heat treatment would enable real-time tracking of RS evolution and γ′ precipitation kinetics, providing deeper mechanistic insights.

## 5. Conclusion

The following conclusions can be drawn from this study:

- The as-built CM247LC processed by PBF–LB contained nanoscale chemical variations, with Cr- and Co-rich regions and complementary Cr-depleted zones enriched in Ni, Al, Ti, Ta, and Hf. These Al-rich clusters are consistent with γ′ precursors and with a spinodal decomposition mechanism, although discrete ordered γ′ precipitates were not crystallographically confirmed.
- Low-temperature heat treatments up to 700 °C promoted elemental partitioning but maintained diffuse interfaces without formation of γ′ precipitates.
- Heat treatments at 750 °C and above caused γ′ precipitation. The precipitate size increased with temperature, with finer γ′ precipitates at 800 °C, fine irregular γ′ at 850 °C, and coarsened γ′ at 1050 °C.
- Residual stress evolution indicated that no significant stress relief occurred at 650 °C, while partial relief (~20 to 40 % reduction) was achieved at 700 °C. This temperature therefore offers potential for partial stress-relief annealing, but only for short durations; longer exposures (e.g., 8 h) resulted in strain-age cracking.
- At 750–1050 °C, residual stresses were effectively relieved with increasing temperature and longer duration, but this coincided with extensive γ′ precipitation and hence extensive strain-age cracking was observed.

## CRediT authorship contribution statement

**Ahmed Fardan:** Writing – original draft, Visualization, Methodology, Investigation, Formal analysis, Conceptualization. **Tatiana Mishurova:** Writing – review & editing, Methodology, Investigation, Formal analysis. **Severin Jakob:** Writing – review & editing, Investigation, Formal analysis. **Guilherme Faria:** Writing – review & editing, Methodology. **Jakob Schröder:** Writing – review & editing, Validation, Methodology, Investigation. **Alexander Evans:** Writing – review & editing, Methodology. **Mattias Thuvander:** Writing – review & editing, Formal analysis. **Håkan Brodin:** Writing – review & editing, Supervision, Conceptualization. **Eduard Hryha:** Writing – review & editing, Supervision, Funding acquisition, Conceptualization.

## Declaration of competing interest

The authors declare that they have no known competing financial interests or personal relationships that could have appeared to influence the work reported in this paper.

## Acknowledgements

This work has been performed in the framework of MAGDA (Materials for green hydrogen fueled gas turbines through additive manufacturing) project, Tailored microstructure control by Additive Manufacturing as enabler for green hydrogen fueled gas turbines (TILDA) project and the Centre for Additive Manufacturing – Metal ($CAM^2$), supported by Swedish Governmental Agency for Innovation Systems (Vinnova). The APT measurements were performed at Chalmers Materials Analysis Laboratory (CMAL). The authors would like to acknowledge Hereon (Geesthacht, Germany) and DESY (Hamburg, Germany), members of the Helmholtz Association HGF, for the provision of experimental facilities at the P61A beamline through proposal I-20240875.

## Appendix A

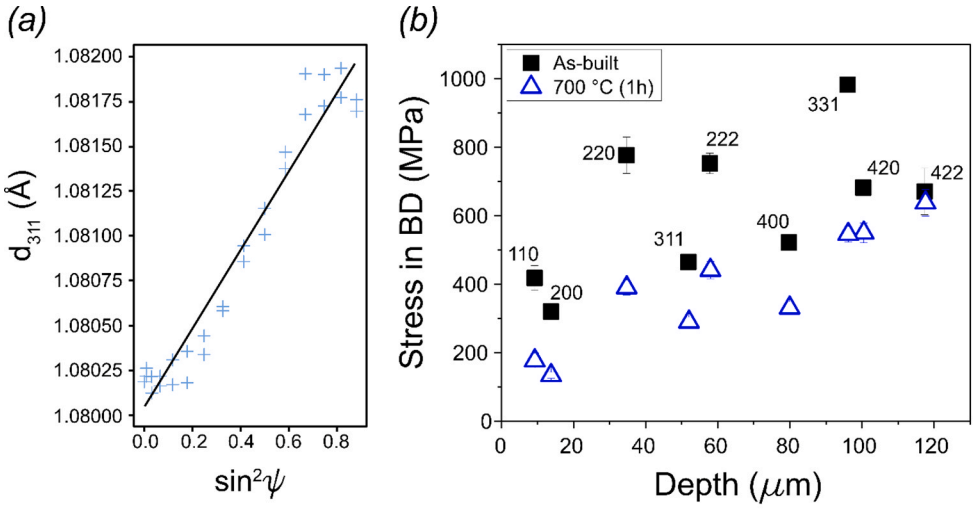


**Fig. A1.** (a) Representative fitting of $d_{311}$ vs for 700°C (1 h) condition, (b) Subsurface depth profile along the build direction (BD) for as-built and 700°C (1 h) condition.

## Appendix B. Supplementary data

Supplementary data to this article can be found online at https://doi.org/10.1016/j.matdes.2026.116955.

## Data availability

Data will be made available on request.

## References


[1] W.E. Frazier, Metal additive manufacturing: a review, J. Mater. Eng. Perform. 23 (2014) 1917–1928, https://doi.org/10.1007/s11665-014-0958-z.

[2] D. Herzog, V. Seyda, E. Wycisk, C. Emmelmann, Additive manufacturing of metals, Acta Mater. 117 (2016) 371–392, https://doi.org/10.1016/j.actamat.2016.07.019.

[3] P.D. Enrique, T. Minasyan, E. Toyserkani, Laser powder bed fusion of difficult-to-print γ′ Ni-based superalloys: A review of processing approaches, properties, and remaining challenges, Addit. Manuf. 106 (2025), https://doi.org/10.1016/j.addma.2025.104811.

[4] A. Fardan, A. Fazi, R.L. Peng, T. Mishurova, M. Thuvander, G. Bruno, H. Brodin, E. Hryha, Fine-tuning melt pools and microstructures: taming cracks in powder bed fusion – laser beam of a non-weldable Ni-base superalloy, Materialia (Oxf) (2024) 102059, https://doi.org/10.1016/j.mtla.2024.102059.

[5] A. Fardan, A. Fazi, J. Schröder, T. Mishurova, T. Deckers, G. Bruno, M. Thuvander, A. Markström, H. Brodin, E. Hryha, Microstructure tailoring for crack mitigation in CM247LC manufactured by powder bed fusion – laser beam, Addit. Manuf. 99 (2025), https://doi.org/10.1016/j.addma.2025.104672.

[6] A. Fardan, J. Gårdstam, H. Brodin, E. Hryha, Overcoming Strain Age Cracking In An Additively Manufactured Non-Weldable Ni-Base Superalloy Through HIP, in: EuroPM 2024, EPMA Publications, Malmö, 2024. https://doi.org/10.59499/EP246281533.

[7] E. Bassini, A. Sivo, P.A. Martelli, E. Rajczak, G. Marchese, F. Calignano, S. Biamino, D. Ugues, Effects of the solution and first aging treatment applied to as-built and post-HIP CM247 produced via laser powder bed fusion (LPBF), J. Alloys Compd. 905 (2022) 164213, https://doi.org/10.1016/j.jallcom.2022.164213.

[8] J.F.S. Markanday, N. D'Souza, N.L. Church, J.R. Miller, J.J.C. Pitchforth, L. D. Connor, S. Michalik, B. Roebuck, N.G. Jones, K.A. Christofidou, H.J. Stone, The relationship between strain-age cracking and the evolution of γ′ in laser powder-bed-fusion processed ni-based superalloys, in: J. Cormier, I. Edmonds, S. Forsik, P. Kontis, C. O'Connell, T. Smith, A. Suzuki, S. Tin, J. Zhang (Eds.), Superalloys 2024, Springer Nature Switzerland, Cham, 2024, pp. 822–835.

[9] S.A.J. Forsik, A.D. Dicus, G.A. Colombo, T. Wang, M.E. Epler, E.T. Connolly, J. Srisuriyachot, A.J.G. Lunt, N. Zhou, Influence of the γ/γ′ misfit on the strain-age cracking resistance of high-γ′ ni and coni superalloys for additive manufacturing, in: J. Cormier, I. Edmonds, S. Forsik, P. Kontis, C. O'Connell, T. Smith, A. Suzuki, S. Tin, J. Zhang (Eds.), Springer Nature Switzerland, Cham, 2024, pp. 908–917.

[10] J.N. DuPont, J.C. Lippold, S.D. Kiser, Welding metallurgy and weldability of nickel-base alloys, Wiley Online Library (2009), https://doi.org/10.1002/9780470500262.

[11] C.T. Sims, N.S. Stoloff, W.C. Hagel, Superalloys II, Wiley-Interscience, New York, NY, United States, 1987.

[12] J.P. Kruth, J. Deckers, E. Yasa, R. Wauthlé, Assessing and comparing influencing factors of residual stresses in selective laser melting using a novel analysis method, Proc. Inst. Mech. Eng. B J. Eng. Manuf. 226 (2012) 980–991, https://doi.org/10.1177/0954405412437085.

[13] P. Mercelis, J. Kruth, Residual stresses in selective laser sintering and selective laser melting, Rapid Prototyp. J. 12 (2006) 254–265, https://doi.org/10.1108/13552540610707013.

[14] A. Ulbricht, S.J. Altenburg, M. Sprengel, K. Sommer, G. Mohr, T. Fritsch, T. Mishurova, I. Serrano-Munoz, A. Evans, M. Hofmann, G. Bruno, Separation of the formation mechanisms of residual stresses in LPBF 316L, Metals (Basel). 10 (2020) 1–15, https://doi.org/10.3390/met10091234.

[15] J. Schröder, A. Evans, T. Mishurova, A. Ulbricht, M. Sprengel, I. Serrano-Munoz, T. Fritsch, A. Kromm, T. Kannengießer, G. Bruno, Diffraction-based residual stress characterization in laser additive manufacturing of metals, Metals (Basel). 11 (2021), https://doi.org/10.3390/met11111830.

[16] J. Schröder, A. Evans, V. Luzin, G. Abreu Faria, S. Degener, E. Polatidis, J. Čapek, A. Kromm, G. Dovzhenko, G. Bruno, J. Keckes, Texture-based residual stress analysis of laser powder bed fused Inconel 718 parts, J. Appl. Crystallogr. 56 (2023) 1076–1090, https://doi.org/10.1107/S1600576723004855.

[17] G. Qiao, B. Zhang, Q. Bai, Y. Dilnoza, Effect of heat treatment on microstructure and residual stress of GH3536 superalloy fabricated by selective laser melting, J. Mater. Eng. Perform. 30 (2021) 8892–8900, https://doi.org/10.1007/s11665-021-06094-4.

[18] W. Zheng, Y. Zhu, Y. Zhang, A. Huang, H. Wang, K. Zhang, Research on heat treatment of nickel–based superalloys by laser powder bed fusion: a review, J. Alloys Compd. 1010 (2025), https://doi.org/10.1016/j.jallcom.2024.177522.

[19] F. Schulz, K. Lindgren, J. Xu, E. Hryha, Gamma prime formation in nickel-based superalloy IN738LC manufactured by laser powder bed fusion, Mater. Today Commun. 38 (2024) 107905, https://doi.org/10.1016/j.mtcomm.2023.107905.

[20] O. Adegoke, J. Andersson, H. Brodin, R. Pederson, Review of laser powder bed fusion of gamma-prime-strengthened nickel-based superalloys, Metals (Basel). 10 (2020) 1–26, https://doi.org/10.3390/met10080996.

[21] D.M. Collins, N. D'Souza, C. Panwisawas, C. Papadaki, G.D. West, A. Kostka, P. Kontis, Spinodal decomposition versus classical γ′ nucleation in a nickel-base superalloy powder: an in-situ neutron diffraction and atomic-scale analysis, Acta Mater. 200 (2020) 959–970, https://doi.org/10.1016/j.actamat.2020.09.055.

[22] K. Dörries, C. Haberland, J. Burow, J. Rösler, B. Gehrmann, C. Somsen, S. Piegert, H. Brodin, Beyond hot cracking: impact of minor elements on a novel Ni-based superalloy for additive manufacturing, in: J. Cormier, I. Edmonds, S. Forsik, P. Kontis, C. O'Connell, T. Smith, A. Suzuki, S. Tin, J. Zhang (Eds.), Superalloys 2024, Springer Nature Switzerland, Cham, 2024, pp. 871–882.

[23] A. Martucci, G. Marchese, E. Bassini, Microstructure and mechanical behaviour of inconel 625 processed by PBF-LB / M, Metals (Basel). (2023), https://doi.org/10.3390/met13040796 Academic.

[24] A. Fardan, J. Schröder, J. Xu, H. Brodin, E. Hryha, Role of scan strategies in modulating micro and macro-cracking in CM247LC processed by powder bed fusion–laser beam, Progr. Addit. Manuf. 11 (2026) 6235–6251, https://doi.org/10.1007/s40964-026-01701-z.

[25] J. Xu, A.S. Shaikh, H. Boyle, S. Kazi, J. Palisaitis, R.L. Peng, E. Hryha, J. Moverare, Strain-age cracking of a γ′-strengthened nickel-based superalloy additively manufactured by laser powder bed fusion, Acta Mater. 312 (2026) 122244, https://doi.org/10.1016/j.actamat.2026.122244.
[26] R. Farla, S. Bhat, S. Sonntag, A. Chanyshev, S. Ma, T. Ishii, Z. Liu, A. Néri, N. Nishiyama, G.A. Faria, T. Wroblewski, H. Schulte-Schrepping, W. Drube, O. Seeck, T. Katsura, Extreme conditions research using the large-volume press at the P61B endstation, PETRA III, J. Synchrotron Radiat. 29 (2022) 409–423, https://doi.org/10.1107/S1600577522001047.
[27] B.C. Giessen, G.E. Gordon, X-ray diffraction: new high-speed technique based on X-ray spectrography, Science 159 (1968) (1979) 973–975, https://doi.org/10.1126/science.159.3818.973.b.
[28] M. Klaus, C. Genzel, Reassessment of evaluation methods for the analysis of near-surface residual stress fields using energy dispersive diffraction, J. Appl. Crystallogr. 52 (2019) 94–105, https://doi.org/10.1107/S1600576718018095.
[29] V. Hauk, Structural and residual stress analysis by nondestructive methods, Elsevier Science (1997), https://doi.org/10.1016/B978-0-444-82476-9.X5000-2.
[30] C. Genzel, Formalism for the evaluation of strongly non-linear surface stress fields by X-ray diffraction performed in the scattering vector mode, Phys. Status Solidi (a) 146 (1994) 629–637, https://doi.org/10.1002/pssa.2211460208.
[31] P61A Toolkit Documentation, P61A Toolkit Documentation, (n.d.). https://hereon-gems.github.io/P61AToolkit/ (accessed September 11, 2025).
[32] T. Gnäupel-Herold, ISODEC: software for calculating diffraction elastic constants, J. Appl. Crystallogr. 45 (2012) 573–574, https://doi.org/10.1107/S0021889812014252.
[33] S. Ma, P. Rangaswamy, B.S. Majumdar, Microstress evolution during in situ loading of a superalloy containing high volume fraction of γ′ phase, Scr. Mater. 48 (2003) 525–530, https://doi.org/10.1016/S1359-6462(02)00504-3.
[34] W. Lefebvre, F. Vurpillot, X. Sauvage, Atom Probe Tomography: Put Theory Into Practice, Academic Press, London, 2016.
[35] J. Xu, F. Schulz, R.L. Peng, E. Hryha, J. Moverare, Effect of heat treatment on the microstructure characteristics and microhardness of a novel γ′ nickel-based superalloy by laser powder bed fusion, Results Mater. 12 (2021) 100232, https://doi.org/10.1016/j.rinma.2021.100232.
[36] J. Xu, H. Brodin, R.L. Peng, V. Luzin, J. Moverare, Effect of heat treatment temperature on the microstructural evolution of CM247LC superalloy by laser powder bed fusion, Mater. Charact. 185 (2022) 111742, https://doi.org/10.1016/j.matchar.2022.111742.
[37] J.F.S. Markanday, K.A. Christofidou, J.R. Miller, E.R. Livera, N.G. Jones, E. J. Pickering, W. Li, Y. Pardhi, C.N. Jones, H.J. Stone, The microstructural evolution of CM247LC manufactured through laser powder bed fusion, Metall. Mater. Trans. A Phys. Metall. Mater. Sci. (2023), https://doi.org/10.1007/s11661-022-06939-0.
[38] A. Fardan, J. Gårdstam, E. Oscarsson, H. Brodin, E. Hryha, Impact of hot isostatic pressing on microstructure evolution and creep performance of powder bed fusion–laser beam processed CM247LC, Adv. Eng. Mater. (2025), https://doi.org/10.1002/adem.202500691.
[39] C.K. Sudbrack, R.D. Noebe, D.N. Seidman, Direct observations of nucleation in a nondilute multicomponent alloy, Phys. Rev. B Condens. Matter Mater. Phys. 73 (2006) 1–4, https://doi.org/10.1103/PhysRevB.73.212101.
[40] H. Zhao, B. Gault, D. Ponge, D. Raabe, F. De Geuser, Parameter free quantitative analysis of atom probe data by correlation functions: application to the precipitation in Al-Zn-Mg-Cu, Scr. Mater. 154 (2018) 106–110, https://doi.org/10.1016/j.scriptamat.2018.05.024.
[41] F. De Geuser, B. Gault, Metrology of small particles and solute clusters by atom probe tomography, Acta Mater. 188 (2020) 406–415, https://doi.org/10.1016/j.actamat.2020.02.023.
[42] J. Zhang, R.F. Singer, Effect of hafnium on the castability of directionally solidified nickel-base superalloys, zeitschrift fuer metallkunde/materials research and advanced, Techniques 93 (2002) 806–811, https://doi.org/10.3139/146.020806.
[43] O. Adegoke, C. Kumara, M. Thuvander, F. Deirmina, J. Andersson, H. Brodin, P. Harlin, R. Pederson, Scanning electron microscopy and atom probe tomography characterization of laser powder bed fusion precipitation strengthening nickel-based superalloy, Micron 171 (2023) 103472, https://doi.org/10.1016/j.micron.2023.103472.
[44] S.S. Babu, M.K. Miller, J.M. Vitek, S.A. David, Characterization of the microstructure evolution in a nickel base superalloy during continuous cooling conditions, Acta Mater. 49 (2001) 4149–4160, https://doi.org/10.1016/S1359-6454(01)00314-7.
[45] D.L. Wenzler, K. Bergmeier, S. Baehr, J. Diller, M.F. Zaeh, A novel methodology for the thermographic cooling rate measurement during powder bed fusion of metals using a laser beam, Integr. Mater. Manuf. Innov. 12 (2023) 41–51, https://doi.org/10.1007/s40192-023-00291-w.
[46] T. Furumoto, K. Oishi, S. Abe, K. Tsubouchi, M. Yamaguchi, A.T. Clare, Evaluating the thermal characteristics of laser powder bed fusion, J. Mater. Process. Technol. 299 (2022), https://doi.org/10.1016/j.jmatprotec.2021.117384.
[47] D.A. Porter, K.E. Easterling, M.Y. Sherif, Phase Transformations in Metals and Alloys, CRC Press, 2009.
[48] J.R. Miller, J.F.S. Markanday, S.M. Fairclough, G.J. Wise, C.M.F. Rae, L.R. Owen, D. Stapleton, N. D'Souza, P.A.J. Bagot, H.J. Stone, Gamma prime precipitation in as-deposited Ni-based superalloy IN713LC, Scr. Mater. 239 (2024) 115775, https://doi.org/10.1016/j.scriptamat.2023.115775.
[49] X. Wang, L.N. Carter, B. Pang, M.M. Attallah, M.H. Loretto, Microstructure and yield strength of SLM-fabricated CM247LC Ni-Superalloy, Acta Mater. 128 (2017) 87–95, https://doi.org/10.1016/j.actamat.2017.02.007.
[50] X.P. Tan, D. Mangelinck, C. Perrin-Pellegrino, L. Rougier, C.A. Gandin, A. Jacot, D. Ponsen, V. Jaquet, Spinodal decomposition mechanism of γ′ precipitation in a single crystal Ni-based superalloy, Metall. Mater. Trans. A Phys. Metall. Mater. Sci. 45 (2014) 4725–4730, https://doi.org/10.1007/s11661-014-2506-8.
[51] H.J. Frost, M.F. Ashby, Deformation-Mechanism Maps, Pergamon Press, The Plasticity and Creep of Metals and Ceramics, 1982.
[52] M.E. Kassner, Chapter 11 - γ/γ′ Nickel-Based Superalloys, in: M.E.B.T.-F. of C. in M. and A. (Third E. Kassner (Ed.), Fundamentals of Creep in Metals and Alloys, Butterworth-Heinemann, Boston, 2015: pp. 261–273. https://doi.org/10.1016/B978-0-08-099427-7.00011-6.
[53] R. Gilles, D. Mukherji, D.M. Többens, P. Strunz, B. Barbier, J. Rösler, H. Fuess, Neutron-, X-ray- and electron-diffraction measurements for the determination of γ / γ lattice misfit in Ni-base superalloys, Appl. Phys. A Mater. Sci. Process. 1448 (2002) 1446–1448, https://doi.org/10.1007/s003390201742.
[54] J. Kou, K. Chen, S. Huang, C. Zhai, C. Chiang, Z. Li, Y. Wang, Mapping stress heterogeneity in single-crystal superalloys by novel submicron-resolved X-ray diffraction, Mater. Res. Lett. 3831 (2024), https://doi.org/10.1080/21663831.2024.2341932.
[55] H. Qin, Z. Bi, D. Li, R. Zhang, T.L. Lee, G. Feng, H. Dong, J. Du, J. Zhang, Study of precipitation-assisted stress relaxation and creep behavior during the ageing of a nickel-iron superalloy, Mater. Sci. Eng., A 742 (2019) 493–500, https://doi.org/10.1016/j.msea.2018.11.028.
[56] P.E. Aba-Perea, T. Pirling, M. Preuss, In-situ residual stress analysis during annealing treatments using neutron diffraction in combination with a novel furnace design, Mater. Des. 110 (2016) 925–931, https://doi.org/10.1016/j.matdes.2016.07.078.